Flexible Steering and Conflict Resolution: Pro-Goal/Anti-Goal Gating in *Drosophila* Lateral Accessory Lobes

Chen-Chieh Liao*[1], Ning Chang*, Yi-Shiuan Liu[2,3], Chung-Chuan Lo[1,4#]
[1]Institute of Systems Neuroscience, National Tsing Hua University, Hsinchu, Taiwan
[2]School of Medicine, National Tsing Hua University, Hsinchu, Taiwan
[3]Institute of Bioinformatics and Structural Biology, National Tsing Hua University, Hsinchu, Taiwan
[4]Brain Research Center, National Tsing Hua University, Hsinchu, Taiwan

*: These authors contributed equally
#: Corresponding author

Keywords
Connectome, steering control, navigation, Drosophila, modeling, conflict, avoidance behavior

Abstract

Navigation comprises multiple processes: sensory integration, position estimation, decision, and finally, motor command generation, which is the control problem. Previous studies discovered that PFL3 neurons compute a heading-goal error and directly project to the descending neurons that generate the steering commands. Yet, this direct pathway is necessary but not sufficient for the flexible control required to pursue goal while avoiding threats and resolving conflicts. Using the Drosophila connectome and circuit modeling, we uncover a layered control architecture in the lateral accessory lobes (LAL) that arbitrates between goal pursuit and stimulus-driving overrides. First, a dorsal pathway that forms a dominant indirect "pro-goal" push-pull circuit that amplifies left-right asymmetries. Second, a faster ventral pathway forms an "anti-goal" circuit that recruits and inverts the pro-goal circuit to redirect movement, and only engages when a goal is present. The architecture also resolves two symmetry challenges: Rear Stalemate (goal 180 behind) and Front Stalemate (threat dead ahead), by rapidly amplifying tiny perturbations into decisive turns. Together, these motifs instantiate comparator, override, and gating principles in a compact neural controller, yielding testable predictions for insect motor control and design rules for bio-inspired, embodied intelligence.

Introduction

Navigating through complex and dynamic environments is a fundamental cognitive ability that supports survival across the animal kingdom [1–3]. To reach desired locations and avoid threats, an animal must integrate multiple sources of information: it must estimate its own position and heading [4–7], construct internal maps of its environment [8], identify and represent behavioral goals [9–11] and ultimately generate motor commands to steer its body toward those goals[12,13]. Therefore, navigation is not merely about computing a destination, but also involves challenges in neural control: transforming internal states [14] and external sensory cues into motor outputs that are **flexible**, **adaptive**, and **robust** in the face of uncertainty or conflicting drives[15–17].

Each of these stages, from spatial encoding to motor execution, depends on specialized neural circuits. Much of our current understanding of spatial representations comes from studies in rodent models, where place cells, grid cells, and head-direction cells provide detailed maps of environmental and body-centered coordinates [7,18–20]. However, the full navigation process also requires **decision-making and control systems** to convert these representations into movement. Investigating these later stages has been challenging in mammals due to the complexity and inaccessibility of distributed brain circuits.

In contrast, the fruit fly, Drosophila melanogaster, provides an opportunity to study navigation and motor control at the single-cell level. Although analogs of place and grid cells have not yet been identified in flies, the availability of powerful genetic tools and brain connectomes, such as FlyCircuit [21,22], hemibrain [23], and FlyWire [24], enables high-resolution circuit dissection. Recent studies have elucidated how flies encode head direction via a ring attractor mechanism [25–30], how synaptic plasticity contributes to flexible encoding [31–33], how wind, heading and motor direction are integrated through vector operation in the central complex [34–37], and how the central brain and the descending neurons generate motor responses [38–43].

Importantly, attention has begun to shift from representation to action. In addition to extensively studied visuomotor control of *Drosophila* [44,45], recent studies investigated goal-directed steering. Neurons known as PFL3 receive inputs encoding current heading direction (via the protocerebral bridge) and internal goal direction (via FC2 neurons) [36]. By summing these signals, PFL3 neurons encode the angular difference between heading and goal, effectively computing a "directional error signal [36]." Their outputs then drive descending neurons (DNs), which in turn initiate turning movements to reduce this error and align the fly with its goal [35,36]. This model provides a simple and elegant solution to the problem of steering, echoing the sensorimotor principles proposed by Valentino Braitenberg in his classic "Vehicles" [46].

However, real-world navigation involves far more than steering toward a static goal. Effective control systems must handle **conflicts, interruptions, and physical contingencies**. Aversive stimuli near the goal may require a temporary retreat. Obstacles may trigger detours. Injuries or body dynamics may distort motor responses. Sensory symmetry, such as when an aversive stimulus lies directly in front of the fly [35], may lead to neural stalemates. In such cases, the system must not only compute an error signal, but must **adapt, override, or resolve competing drives**. This requires a control architecture that is both goal-directed and **flexibly reconfigurable**.

In this study, we hypothesize that such flexible control emerges from circuit motifs within the lateral accessory lobe (LAL) [47,48], a brain region interposed between PFL3 and descending neurons. Using the Flywire and hemibrain connectome databases, we identify a network of direct, indirect, recurrent and feedforward pathways in the LAL. Through in-depth analysis and computer simulations, we find that these circuits implement two distinct steering modes: a **pro-goal response** that turns the fly toward a target, and an **anti-goal response** that turns it away from aversive stimuli near the goal. Furthermore, the circuit architecture can resolve symmetrical input conditions: rear stalemate and front stalemate, through mechanisms that amplify small perturbations into decisive actions.

By modeling these circuits, we demonstrate that LAL enables a compact yet powerful control strategy that balances goal pursuit with environmental contingencies. The architecture mirrors core principles of control theory and behavioral arbitration, such as comparator circuits, override relays, and layered behavioral hierarchies, and may represent a scalable strategy for robust action selection. These findings not only shed light on neural control in *Drosophila*, but also offer design principles for bio-inspired embodied agents with minimal yet adaptive neural systems.

Results

The goal-directed steering behavior and associated LAL neurons

We investigated the neural circuits underlying goal-directed steering behavior, in which a goal is initially offset from the fly's head direction, requiring the fly to turn its body until it becomes aligned with the goal (Fig. 1A). Previous work identified PFL2 and PFL3 neurons as encoding the head-goal offset ($\Delta\theta$) and projecting downstream descending neurons (DNs) that drive turning behavior (Fig. 1B).

By analyzing connectomic data, we found that this previously identified circuit represents only a partial picture of the goal-directed steering control. Using the Flywire database, we identified a cluster of lateral accessory lobe (LAL) neurons that receive strong input from PFL2/3, and, in turn, form dense synaptic connections with the turning-related descending neurons DNa01-04. Among these, DNa02 is known to play a crucial role in mediating turning movements[35,38,40,49], while DNa01, 03 and 04 were included in our analysis because of their strong connectivity with DNa02.

The selected LAL neurons, LAL018, 014, 121, 122, 046, 040, 010 and 126, constitute the first set of neurons in our proposed model (Fig. 1C). Cross-validation using the hemibrain database confirmed that most of these neurons are among the most strongly connected LAL neurons between PFL2/3 and DNa01-04, except for a few that project contralaterally (and Supplementary Figs. 1). Because the hemibrain dataset covers only one hemisphere of the brain (except for a few central complex neuropils), our model was primarily developed based on the bilateral connectome data from the Flywire.

We also identified strong synaptic connections between additional neurons and the neurons in the first set. Although receiving no PFL2/3 input, the LAL017 and 153 form strong connections to and from the neurons in the first set, including LAL121, 122, 010 and 040. The LAL073 receives inputs from PFL2 and interconnected with LAL121, 153 and 040.

These three neurons (LAL017, 153 & 073) may also participate in the steering contorl and were included in the model (Fig. 1D). The entire circuit modeled in the present study, including the input (PFL2 & PFL3) and output descending (DN) neurons, consists of 12 PFL2 neurons, 24 PFL3 neurons, 22 LAL neurons (bilateral LAL 010, 014, 017, 018, 040, 046, 073, 121, 122, 126, 153), and 8 DNa neurons (bilateral DNa 01-04)(Fig. 1E). Note that LAL122 has two neurons on each side. All these neurons form 236 connections (Supplementary Table 1) if we only consider the connections formed by more than 5 synapses, considering the potential error in automated identification. These neurons not only form feedforward connections with turning-related descending neurons but also interconnect with one another. Some neurons project ipsilaterally, some contralaterally, and some bilaterally. These connections form an intricate circuit (Fig. 1F). To further elucidate their function, we analyzed the inputs to the circuit and discovered that in addition to the known PFL3/PFL2 inputs, some neurons also receive inputs from IPS (Supplementary Figs. 2), which can be traced all the way to the optical lobe as well. The former pathway starts from the medulla, passing through AOTU, BU, EB, PB, FB, and then reaching LAL (Fig. 1G top). The latter pathway also starts from the medulla, but passes through LOP, LPTC, IPS and then reaches LAL (Fig. 1G bottom). We referred to the former pathway as “dorsal” and the latter as “ventral” based on their relative locations in the brain. Note that the naming does not imply their functional relevance with the classic dorsal and ventral visual pathways described in mammalian cortices. The two distinct pathways form synaptic connections with different neurons in LAL, suggesting that the circuit can be divided into two subcircuits serving distinct functions. By extensively analyzing their connections and performing computer simulations, we were able to sort out their functional relationships. The full circuits can be classified into two subcircuits based on the input pathways: the pro-goal and the anti-go circuit, which primarily receive projections from the dorsal and ventral pathways, respectively (Fig. 1H). Excitatory neurons in the pro-goal circuit either excite the other pro-goal neurons and/or the descending neurons ipsilaterally. In contrast, the inhibitory neurons in the pro-goal circuit inhibit other excitatory or descending neurons contralaterally. Both effects facilitate the response that turns the body toward the goal. In contrast, neurons in the anti-goal circuit make their connections in a way opposite to the pro-goal neurons, leading to effects that suppress the pro-goal response and facilitate the response that turns the body away from the goal direction (Fig. 1H). For ease of understanding, we rename the neurons based on their upstream input pathway (V for ventral and D for dorsal) and the tentative function (E for excitatory and I for inhibitory) predicted in the FlyWire database. The readers are referred to Table 1 for the mapping between the FlyWire neuron IDs and the functional names used in this paper.

Table 1: Neuron ID (Flywire) and Functional Name (this paper) Mapping

Neuron ID in FlyWire	ID in the present paper	Circuit classification / Tentative functions	Neuron ID in FlyWire	ID in the present paper	Circuit classification / Tentative function
LAL010	DE1	pro-goal / excitation	LAL073	DI4	pro-goal / inhibition
LAL014	DE2	pro-goal / excitation	LAL153	VE1	anti-goal / excitation
LAL018	DE3	pro-goal / excitation	LA017	VE2	anti-goal / excitation
LAL040	DI1	pro-goal / inhibition	LAL122	VI1	anti-goal / inhibition

LAL121	DI2	pro-goal / inhibition	LAL046	VI2	anti-goal / inhibition
LAL126	DI3	pro-goal / inhibition			

The pro-goal circuit

The pro-goal circuit consists of DE1 (LAL010), DE2 (LAL014), DE3 (LAL018), DI1 (LAL040) DI2 (LAL121), DI3 (LAL126) and DI4 (LAL073) (Fig. 2A). DE1-3 are tentatively cholinergic neurons and they all receive inputs from the contralateral PFL3 and project to the ipsilateral descending neurons (DNs) (Fig. 2A). Interestingly, DE1 and DE2 form weak mutual connections and they both project to DE3. These three neurons form an excitatory core (EC) and their responses to the PFL3 inputs are amplified through the excitation connections between them. DI1 and DI2/DI3/DI4, on the other hand, are tentative GABAergic and Glutamatergic inhibitory neurons, respectively. They also receive strong input from the contralateral PFL3 neurons and inhibit the contralateral DNs and EC (Fig. 2A).

We performed simulations for this pro-goal circuit in an open-loop setting, where the input (goal-head offset) was a constant and was not influenced by the output of the descending neurons. The reason for using open-loop simulations was to investigate the steady-state response of the circuit and gain a better understanding of the role of each neuron. We set PFL3 neuron fire rates so that they represented a 90° goal-head offset ($\Delta\theta$=90°, the goal is on the left of the head direction). The input from PFL3 neurons was able to trigger the separation of the left and right firing rates for all downstream neurons (Fig. 2B and Supplementary Figs. 3). In about 100 ms, the DNa02_L became significantly more active than DNa02_R, characterizing the initiation of a left-turning behavior and reduction of the goal-head offset.

Next, we investigated the roles of individual components in the pro-goal circuit. One interesting question is about the purpose of the excitatory core formed by DE1, DE2 and DE3. Since PFL3 neurons already innervate the descending neurons, why do we need an indirect pathway mediated by the excitatory core? Our test revealed that a potential function of the excitatory core is to provide an auxiliary drive to the descending neurons. Without the excitatory core (EC), the left-right firing rate difference of the descending neurons Δr_{DNa02} is much smaller than when the core is present (Fig. 2C and Supplementary Figs. 4). Note that the relative connection strengths were determined by the number of synapses from the database; therefore the importance of EC did not result from the choice of tuning parameters but was the consequence of observed connectivity. We systematically tested the full model for different $\Delta\theta$s, and computed the average Δr_{DNa02} over 50 trials. The result showed the effect of the EC on Δr_{DNa02} presents in small and large offsets (Fig. 2D). We further performed a cleaner test by simulating an isolated circuit that only contains unilateral EC, its upstream PLF3 and downstream DNa02 from the rest of the model. This way, we could test EC's effect on the DNa02 without interference from other neurons. We confirmed that the direct input from PFL3 and PFL2 to DNa02 was not sufficient to activate it. The additional input from EC played a vital role in activating DNa02 (Fig. 2E).

In addition to EC, the pro-goal also contains contralaterally projecting inhibitory neurons DI1-DI4. Note that the turning rate depends on the firing rate difference between the left and right descending neurons (Δr_{DNa02}). When boosting the unilateral descending neurons for turning, the circuit also needs to inhibit the descending neurons on the other side to

increaseΔr_{DNa02}. This is where DI1-DI4 come into play. To verify it, we tested the role of the contralaterally projecting inhibitory neurons DI by removing it, and we observed that the right DNa02 was not suppressed, leading to highly activated DNa02R and DNa02L (Fig. 2F and Supplementary Figs. 5). We performed 50 trials and verified that Δr_{DNa02} was significantly reduced without DI1. We also performed the same test for DI2 and obtained the same result (Fig. 2G & 2H). As for the third contralaterally projecting inhibitory neuron DI3, its effect is similar but much weaker than DI1 and DI2. Our tests showed that removing DI3 or DI4 produced minor effects on the responses of DN02 (Supplementary Figs. 22). Therefore, we did not include these two neuron types in the subsequent analyses.

In summary, the pro-goal circuit forms a "push-pull" mechanism that amplifies the pro-goal responses by exciting ipsilateral DNs and inhibiting contralateral EC and DNs.

Rear Stalemate

The pro-goal circuit exhibits an inherent problem: the goal-directed rotation becomes very slow when the goal is behind it ($\Delta\theta$ ~180°), and is immobilized when the goal is exactly 180° from the head direction ($\Delta\theta$ =180°). We refer to this problem as "Rear Stalemate" (Fig. 3A). Rear Stalemate occurs because the firing rate difference between PFL3R and PFL3L reduces when $\Delta\theta$ >90° and becomes zero at $\Delta\theta$ =180° (Fig. 1B). This issue was investigated recently and another set of neurons, PFL2s, were shown to be involved in resolving Rear Stalemate[35]. Unlike PFL3_R and PFL3_L neurons, which project to the contralateral side, PFL2_R and PFL2_L project to several LAL neurons and DNa03 bilaterally, with firing rates highest at $\Delta\theta$ =180° and monotonically decreasing when $|\Delta\theta|$ decreasing (Fig. 1B). This input provides an extra driving force that compensates for the weak PFL3 input and increases the turning velocity at $\Delta\theta$ ~180°. However, including PFL2 in the system does not fully resolve the Rear Stalemate because at $\Delta\theta$=180°, because the input from PFL3 is symmetric, and so is PFL2 (Fig. 3B). To break the Rear Stalemate at $\Delta\theta$=180°, DNa02 and DNa03 need asymmetric inputs to tip the balance. We verified, as expected, the noise played an important role, as a higher noise level induces larger $|\Delta r_{DNa02}|$ (Fig. 3C and Supplementary Figs. 6). We further discovered that other neurons, such as EC and DIs, were also important. We removed EC or DI2 and $|\Delta r_{DNa02}|$ drastically reduced (Fig. 3D and Supplementary Figs. 7). We performed a systematic test of the roles of PFL2, EC and DIs in resolving Rear Stalemate and calculated the averaged sum of DNa02_L and DNa02_R, Σr_{DNa02} $(= r^R{}_{DNa02} + r^L{}_{DNa02})$, and difference between DNa02_L and DNa02_R, $|\Delta r_{DNa02}|$ $(= |r^L{}_{DNa02} - r^R{}_{DNa02}|)$ over 50 trials. We used a large noise level (s.t.d. = 0.07) to magnify their effects for comparison purposes (Fig. 3E). We found that the full model gives rise to the largest $|\Delta r_{DNa02}|$, while removing any of the three components (EC, DI2, PFL2) leads to a smaller Δr_{DNa02}, indicating the weaker ability to break the Rear Stalemate (Fig. 3E left). On the other hand, we can also test the effect of the three components by adding each one to a bare model (BM), which is the full model without EC, DI and PFL2. The test showeed that any of the components alone cannot produce a $|\Delta r_{DNa02}|$ as large as the full model, indicating the importance of including all three components in Rear Stalemate (Fig. 3E right). By analyzing these two test results (loss-of-function from a full model and gain-of-function from a bare model), we concluded that the maximum $|\Delta r_{DNa02}|$ can only be achieved by the collaborative effect of all three components (EC, DI and PFL2). We visualized this effect by showing how

$|\Delta r_{DNa02}|$ and Σr_{DNa02} changed when each component was added to a bare model one by one (Fig. 3F): (1) adding EC to the bare model (BM+EC) strongly increased bilateral r_{DNa02} (Σr_{DNa02}) but not $|\Delta r_{DNa02}|$. (2) Next, adding DI (BM+EC+DI) slightly increased $|\Delta r_{DNa02}|$ but Σr_{DNa02} severely reduced due to the inhibition from DI. One should note that the small Σr_{DNa02} limited the maximum value of $|\Delta r_{DNa02}|$, which should be always smaller than $|\Delta r_{DNa02}|$. (3) Finally, we added PFL2 to complete the full model. PFL2 strongly raised Σr_{DNa02}, allowing DI to further increase $|\Delta r_{DNa02}|$. We emphasize the necessity of two excitatory neuron groups (EC and PFL2). With only one excitatory group, the excitatory drive was not sufficient to counter the inhibition from DI. If only one excitatory group existed (BM+PFL2+DI or BM+EC+DI), Σr_{DNa02} became small, limiting the value of $|\Delta r_{DNa02}|$. We noticed that the co-existence of PFL2 and EC exhibited a "nonlinear" effect: when only one excitatory group paired with DI, $|\Delta r_{DNa02}|$ was much smaller than half of when both groups are included. The nonlinear effect resulted from the interaction between PFL2 and EC subcircuits. PFL2 projected to DNa03, which fed back to DE2 (part of EC). DE2 in turn projected to DNa02, which is the main driver neuron for the turning response. Therefore, activated PFL2 enhanced the output of EC, which strongly activated DNa02 (Fig 3G). Without EC, PFL2's effect on DNa02 was greatly reduced.

In summary, the Rear Stalemate represents a symmetry-induced indecision and it can be resolved by noise-driven symmetry breaking and winner acceleration with a helper circuit (PFL2 + EC + DI).

The anti-goal circuit

We discovered that a set of neurons projects to DNs in a manner opposite to the pro-goal circuit. The circuit is mainly formed by VE1 (LAL153, cholinergic), VE2 (LAL017, choloinergic), VI1 (LAL122, glutamatergic), and VI2 (LAL046, GABAergic), which receive weak or no inputs from PFL2 and PFL3 (Fig. 4A). Instead, VE1, VE2 and VI2 receives strong inputs from unilateral IPS (inferior posterior slope), which potentially carry visual information[38,50]. VE1 is predicted to be cholinergic, and it projects to the contralateral DN (Fig. 4A, path 1). Therefore, a strong visual input from the right side may elicit a left turn via VE1, and vice versa. Moreover, VE1 projects to the contralateral VE2 and VI1 (Fig 4A, path 2). The latter inhibits DNs ipsilateral to the activated VE1 (Fig. 4A, path 3). Moreover, VI2 receives ipsilateral IPS inputs (similar to VE1) and inhibits ipsilateral DNs (Fig 4A, path 4). Both inhibitory projects facilitate the turning driven by VE1. We found that the anti-goal not only directly manipulates the descending neurons, but also recruits neurons in the pro-goal circuit for generating the anti-goal responses. VI1 and VI2 inhibit EC and DI opposite to the direction of anti-goal turning (Fig 4B, paths 5 & 6), respectively. VE1 and VE2, on the other hand, activate EC and DI in the same direction as the anti-goal turning (Fig 4B, paths 7, 8), respectively. We speculated that these connections enable the anti-goal circuit to override the pro-goal circuit, thereby resolving conflicts between them. On the other hand, we also found that VI1 provides a feedback inhibition to the contralateral VE1, which seems to suppress the anti-goal response (Fig. 4A, path 9). We speculated that this connection serves to prevent VE1 from over-activating in response to visual input. We verify the speculations by performing the simulation of the circuits. We first demonstrated the effect of this anti-goal circuit by setting the goal to the left ($\Delta\theta$=90°) of the head direction. We activated the left VE1, VE2 and VI2, mimicking the left IPS input they receive. The unilateral activation successfully produced a higher right DNa02 activity than the left one, indicating an anti-goal

response (Fig. 4C and Supplementary Figs. 8). We verified that both VE1 and VI1 are crucial for the anti-goal function. By lesioning VE1 (removing all its outputs), the IPS input failed to reverse Δr_{DNa02}, or the rotational direction (Fig. 4D and Supplementary Figs. 9). Lesion of VI1 produces higher right DNa02 than the left one (Δr_{DNa02}>0), but the firing rate difference is small, indicating a very weak anti-goal response (Fig. 4E and Supplementary Figs. 10). We also tested the effect of VE2 and discovered that lesioning it causedd a minor changes to the DNa02, while over-activating it greatly decreased Δr_{DNa02}, or a reduced anti-goal response (Fig. 4F and Supplementary Figs. 11). The test suggested VE2's main effect is to suppress the anti-goal response.

We further discovered a surprising and counterintuitive phenomenon: the anti-goal response requires the coexistence of pro-goal input from PFL3 and PFL2. By removing the pro-goal input, the same anti-goal input from IPS fails to produce an anti-goal response (Δr_{DNa02}>0) (Fig. 4G and Supplementary Figs. 12). Intuitively, an anti-goal input needs to overcome the pro-goal response when the pro-goal input co-exists. Therefore, removing pro-goal input should make the anti-goal response easier. To investigate this phenomenon, we make a control experiment by removing connections from the anti-goal circuit to the pro-goal circuit so that the two circuits run independently (Fig. 4H and Supplementary Figs. 13). The results indicate that the anti-goal circuit cannot outcompete the pro-goal circuit when the two operate independently, and the anti-goal-to-pro-goal connections are necessary for an anti-goal response. This counterintuitive phenomenon stems from an intricate mechanism in which the anti-goal circuit recruits the pro-goal circuit and reverses it (Fig. 4B and Fig. 4I). The anti-goal circuit utilizes the fact that when a pro-goal signal drives a rotation, both the left and right sides of the circuit receive inputs. Normally, when the fly only performs the pro-goal turning (left turn for example), the turning side of the circuit receives larger input and suppresses the response of the non-turning side (right side) via lateral inhibition (left DI to right EC and DNs) (Fig. 4I left). When an anti-goal response is required in this case, the anti-goal circuit inhibits the left side of the pro-goal circuit, which releases the inhibition on the right pro-goal circuit. Moreover, the anti-goal also adds a small excitation to the right DNs, amplifying the response in the right side and triggering a right anti-goal turn (Fig. 4I middle). Without any pro-goal input, the small excitation that the anti-goal exerts on the DNs (right) would not be sufficient to trigger any turning behavior (Fig. 4I right). This explains why anti-goal requires the pro-goal circuit to perform an anti-goal turning.

One may think that the anti-goal circuit should be able to activate an anti-goal response without the help of the pro-goal circuit as long as the anti-goal input is sufficiently strong. We argue that this is not the case due to the function of the VI1, which provides feedback inhibition to VE1 (Fig. 4A, path 9) to suppress its response. We verified this argument by removing the VI1à VE1 connections in the no pro-goal input condition and found that the circuit develops a stronger anti-goal response (larger Δr_{DNa02}) than the original circuit (Fig 4J and Supplementary Figs. 14). Next, we performed a systematic test by varying the anti-goal input strength under different lesion conditions, including removing the pro-goal input, the VI1→VE1 connections, or both (Fig. 4K). We found that in the full model, there is a threshold for the anti-goal input strength to trigger an anti-goal response. Removing VI1→VE1 lowered the threshold (Fig. 4K, from blue to green curves). Removing the pro-goal input abolished the DN response (Δr_{DNa02}) for all anti-goal input strengths. But the anti-goal response can be partially rescued by removing the VI1→VE1 connections. We concluded that the intricate anti-goal circuit, with the help of VI1→VE1 connections, serves as a condition detector. The circuit only functions when the goal input is presented. The test

also verified the function of VE2, which works as a brake to the anti-goal response. Overactivating VE2 eliminated the anti-goal response at all input strengths (Fig. 4K).

In summary, the anti-goal circuit works via three mechanisms: 1. Direct inhibition/Excitation. 2. Recruitment and reversal of the prog-goal circuit. Specifically, the anti-goal circuit hijacks the pro-goal cirucuit by repurposing the pro-goal circuit and generate strong output in the opposite direction. 3. Brake / output limiter. The anti-goal excitatory neurons recruit inhibitory feedback, creating a self-limiting loop. Putting it all together, the anti-goal circuit resembles a "low-power override controller" in engineering systems, which do not directly steer the actuators, but redirect or invert the main controller. If the main controller is not activated (i.e., no goal is presented), there is nothing to override.

Front Stalemate

Similar to the pro-goal circuit, the anti-goal circuit also faces a challenge: the front stalemate. When both the goal and the aversive stimulus are perfectly aligned with the head direction, both sides of the anti-goal circuit will receive inputs of the same strength, which leads to a stalemate condition (Fig. 4L). We tested the response of system in this stalemate condition and found that as long as noise was sufficiently large, the anti-goal circuit can still overcome the goal-attraction drive from the pro-goal circuit and initiate an anti-goal response (Fig. 4M and Supplementary Figs. 15).

The closed-loop simulations

After examining the dynamics of the LAL neural circuit in the open-loop simulation, we need to check whether the LAL neural circuit is capable of performing the proposed pro-goal and anti-goal functions in the closed-loop setup, in which the output of the circuit (descending neurons firing rate) changes the heading and the PFL2/3's activity is updated based on the new heading (Fig. 5A)(See Materials and Methods for details). We first tested the system in a pro-goal task with $\Delta\theta = 90°$. The circuit was able to quickly bring the heading to the goal direction in about 1s, consistent with the time scale of the turning behavior of real flies (Fig. 5B and Supplementary Figs. 16). The initial large PFL3 input quickly elicited strong descending neuron output (Δr_{DNa02}). As the heading moved close to the goal, Δr_{DNa02} quickly reduced and dropped to 0 when $\Delta\theta = 0$. It is important to reexamine the roles of each neuron in the pro-goal task in the closed-loop setup. To this end, we performed lesion tests by removing individual neurons from the circuit. We found that, as described in the open-loop tests above, the excitatory core neurons exerted an auxiliary drive. Removing any of the excitatory core neurons led to an undershot rotation, and the time it took to reach the goal drastically increased (Fig. 5C and Supplementary Figs. 17). Removing any lateral-inhibition neurons also caused similar effects (Fig. 5D and Supplementary Figs. 17), in which the rotational speed was greatly reduced. Close examination of the firing rate traces of the descending neurons revealed an interesting phenomenon. Although removing excitatory core neurons or the lateral inhibition neurons led to similar behavioral effects, the underlying neural mechanisms are distinct. Removing the excitatory core neurons resulted in weakly activated DNa02 on both sides, leading to a small Δr_{DNa02}. In contrast, the small Δr_{DNa02} resulted from removing the inhibitory neurons stemmed from failing to inhibit both DNa02.

Next, we performed the anti-goal task in the closed-loop setup (Fig. 5E). In each trial, we started with a pro-goal movement ($\Delta\theta = 90°$) by providing heading and goal direction input to PFL2 and PFL3 neurons. After 200ms, we turned on the unilateral IPS input to the model

and verified that the turning could be reversed (Fig. 5F and Supplementary Figs. 18). We further performed the lesion tests and verified that removing VE1 abolished the anti-goal response (Fig. 5G left and Supplementary Figs. 19A). Lesioning VI1 moderately reduced the speed (-107.88 °/s vs. -141.29 °/s in the original model), while strengthening the input (from IPS) to VE2 by three folds significantly slowed down the anti-goal rotational speed (Fig. 5G middle & right and Supplementary Figs. 19B, C). The results were in consistent with the open-loop tests (Fig. 4D-F). We conducted a systematic test with various initial goal-head offset ($\Delta\theta$) and tested whether an anti-goal rotation can always be triggered (Fig. 5H). We discovered that although the answer was positive, there were thresholds of the anti-goal input strength that could trigger the anti-goal responses. The threshold was depended on the initial $\Delta\theta$ with a relationship that reflected the strength of the pro-goal drive, which is roughly proportional to the sum of $r_{PFL2R} + r_{PFL2L}$ and $|r_{PFL3R} - r_{PFL3L}|$ (Fig. 5I). The result indicated the nature of conflict-resolution in the anti-goal task, in which the signal of an counter action (anti-goal) needs to be as strong as the un-wanted action (pro-goal) to overcome it.

We next tested Real and Front Stalemate in the closed-loop setup. We started the pro-goal task at $\Delta\theta = 180°$ and verified that the full model was capable of resolving Real Stalemate and started a pro-goal rotation in a few seconds (Fig. 6A and Supplementary Figs. 20). We also conducted the lesion tests by removing EC, DI1 & DI2 or PFL2. We measured the reaction time, defined as the time when the head angle changed by 1.5° after the onset of the pro-goal input. Removing one or any two of the components led to a significant increase of the reaction time (Fig. 6B), which was in consistent with the results from open-loop tests. We next tested Front Stalemate by setting both goal direction and the aversive stimulus at the front of the head and measured the response time. The model was able to overcome the pro-goal response and started to turn away from the aversive stimulus in a few hundreds of miliseconds (Fig. 6C and Supplementary Figs. 21). Similarly, lesion tests revealed the results that are consistent with the open-loop tests (Fig. 6D).

Finally, we performed a systematic test to probe the functions of each neuron by lesioning each neuron type one by one in the pro-goal, anti-goal, Rear Stalemate and Front Stalemate tasks. We measured the changes in the $\Delta r_{\mathrm{DNa02}}$, comparing to that of the full model. The test verified the functional assessment presented in the earlier part of this paper (Figure 6E). Notably, removing the EC (DE1-DE3) reduced the response in all tasks, even in the anti-goal and ront stalemate. This was because the anti-goal circuit needed to recruit an activated pro-goal circuit to perform an anti-goal response as we demonstrated previously (Fig 4 G-I). Without EC, the pro-goal circuit had little activity, hence the anti-goal circuit could not perform its function efficiently.

Discussions

The lateral accessory lobe (LAL) of the *Drosophila* brain has been considered a hub for transforming sensory and goal-related input into descending motor commands. By analyzing the connectome and functional motifs within the LAL, we uncovered a set of circuit mechanisms that underlie flexible, context-dependent motor control, including mechanisms for pursuing internal goals and avoiding external threats. Our findings reveal two distinct yet interrelated neural pathways: the pro-goal circuit, which drives goal-directed steering, and the anti-goal circuit, which turns the body away from the goal. We also identified two challenge

conditions: the Rear Stalemate and Front Stalemate, in which the system must resolve symmetry-induced indecision to produce a motor response. These motifs provide a computationally efficient, dynamically adaptive framework for action selection, and resonate with well-established architectures in control theory, digital systems, robotics and even molecular biology.

Pro-goal circuit: Amplification without persistence

The pro-goal circuit receives visual input via the dorsal central complex pathway and operates as a transient amplifier of directional intent. The bilateral set of pro-goal neurons excites ipsilateral descending neurons (DNs) and inhibits their contralateral counterparts, forming a push-full loop. This motif is analogous to transient comparator circuits in engineering, which produce a directional output based on input difference but do not retain memory of past states. This mechanism is in contrast to winner-take-all (WTA) or bistable attractor circuits, which are formed by strong local recurrent excitation and produce hysteresis. In contrast to many other *Drosophila* brain regions, where strongly recurrent excitation is commonly presented, strong recurrent excitation is not discovered in the pro-goal circuit. This is crucial. Otherwise, the system would easily overshoot when the system reaches the goal direction ($\Delta\theta = 0°$) due to hysteresis. Biologically, the pro-goal circuit resembles Rac1-RhoA polarity systems in migrating cells [51,52], where mutual inhibition between signaling modules amplifies slight input differences into robust front-rear polarization.

An intriguing feature of the circuit architecture is that PFL3 neurons project to descending neurons through both a direct and an indirect pathway. The indirect route, mediated via the pro-goal circuit in the LAL, is functionally dominant: silencing this pathway abolishes goal-directed turning, whereas the direct PFL3→DN connection alone is insufficient to drive behavioral output. This raises the question: why retain a weak direct pathway if the indirect pathway is essential? We propose that the direct pathway may serve as a **priming mechanism**, bringing the descending neurons closer to threshold and thereby enabling a faster and more efficient response once the stronger signal arrives via the indirect route. This architecture mirrors feedforward excitation seen in other sensorimotor systems, where early subthreshold input facilitates rapid triggering by later-arriving signals.

Equally important, the indirect pathway provides a critical site for **modulation and behavioral flexibility**. In complex environments, multiple brain systems may compete to steer behavior based on internal goals, sensory threats, or learned contingencies. If PFL3 neurons projected solely to descending neurons, it would be difficult for other circuits, e.g. the anti-goal pathway, to inhibit or override the goal-directed response without broadly suppressing all motor output. The pro-goal circuit thus functions as a "gateable" relay, allowing other circuits to selectively modulate or suppress goal-driven turning without blocking the descending pathway entirely. This separation of command (PFL3) and control (LAL pro-goal circuit) confers a layered architecture in which behavioral responses are not only fast and directionally precise but also highly adaptable to changing motivational and environmental contexts.

Anti-goal circuit: Override control with feedback constraint

In contrast, the anti-goal circuit receives rapid visual input via the ventral IPS pathway and promotes the turning away from the visual stimuli. However, its architecture suggests that it is not a strong independent controller. Rather, it employs three complementary mechanisms:

(1) a direct but push-pull output to DNs, (2) recruitment and reversal of the pro-goal circuit, effectively **hijacking** its output to the opposite direction, and (3) an "internal" brake system formed by a feedback inhibition loop that constraints the anti-goal circuit's own output amplitude.

This architecture mirrors the override systems in robotics and digital control, where a secondary controller cannot act alone but can reverse the polarity of the main controller. The internal brake in the anti-goal circuit is conceptually similar to interlock circuits or current limiters that ensure safety by capping output strength. In molecular biology, this resembles systems such as p53-MDM2 loop [53,54], where a stress response controller (p53) can override normal cell-cycle progression but is tightly regulated via feedback inhibition.

Another notable feature of the anti-goal circuit is the asymmetric interaction between the pro-goal and anti-goal pathways. While the pro-goal circuit does not inhibit the anti-goal circuit, the anti-goal pathway can actively suppress and invert the pro-goal circuit. This asymmetry suggests a functional hierarchy: when both pathways are engaged, the system prioritizes the anti-goal response. In ecological terms, this makes adaptive sense: responding to an immediate threat or aversive stimulus is typically more urgent than continuing to pursue an internal goal. The anti-goal circuit's ability to override the pro-goal drive reflects a built-in bias toward survival-driven behavioral interruption, ensuring that ongoing goal-directed actions can be rapidly halted and reversed when necessary.

It is also important to distinguish the anti-goal response described here from a more general avoidance behavior. The anti-goal circuit does not operate in isolation; it requires the presence of a goal signal from the pro-goal pathway in order to function. In the absence of goal-related input, the anti-goal circuit cannot trigger any response, highlighting its role not as a standalone avoidance mechanism, but as a goal-modulated override system that redirects ongoing goal-directed actions away from an aversive stimulus. In contrast, a pure avoidance response should be able to trigger turning behavior independently of internal goals. Indeed, our connectome analysis reveals that the IPS projects not only to the LAL but also directly to descending neurons, potentially forming a parallel, faster-acting avoidance pathway. This architecture implies a layered defensive system: a fast, goal-independent reflex pathway for urgent avoidance, and a slower, context-sensitive anti-goal pathway that modifies goal pursuit only when necessary. This separation allows the nervous system to flexibly arbitrate between reflexive escape, goal continuation, and goal redirection, depending on internal state and environmental context.

Symmetry breaking in behavioral stalemate

We further examined two behavioral conditions, Rear Stalemate and Front Stalemate, that challenge directional decision-making. In both cases, we observed that the push-pull architecture of the pro-goal and anti-goal circuit plays a crucial role in resolving symmetry.

The symmetry-breaking behavior resembles the metastable states in digital electronics, which linger in uncertain states until random fluctuation resolves them. The behavior is also analogous to the lateral inhibition-based patterning in developmental biology. A direct parallel is found in the Notch-Delta signaling system, where two neighboring cells with equal inputs eventually break symmetry through mutual inhibition and stochastic tipping, resulting in distinct fates [55–57].

Conceptual implications: Shared principle across scales and systems

Taken together, our findings highlight how *Drosophila* LAL implements a modular control architecture that balances goal pursuit with environmental responsiveness. The underlying motifs – symmetry-sensitive push-pull comparators, feedback-limited overrides, and noise-driven decision gates -- recur across biological and engineering systems. These shared patterns suggest that evolution and engineering converge on similar solutions when facing similar problems. What distinguishes the LAL is not merely its ability to compute directional outputs, but its contextual-sensitive integration: the anti-goal circuit only becomes effective in the presence of the goal. This logic mirrors biological systems where signals are contingent on combinatorial context, which is a principle deeply embedded in gene regulation, cell signaling, and decision-making networks across levels of organization.

By tracing these analogies, we argue that the LAL does not merely encode the motor signals, but implements a compact, dynamics conflict-resolution engine, which is an insect-scale example of how compact circuits can resolve symmetry, arbitrate competing drives, and generate adaptive behaviors. These findings may inspire future efforts to build bio-inspired, neuromorphic control systems that mimic these principles to navigate complex environments with minimal hardware.

Limitations and Future Directions

As with any modeling study, there are important limitations that should be addressed in future work. First, our circuit model assumes that all neurons operate under a simplified and uniform dynamical regime, using sigmoid activation functions to approximate their input–output relationships. While this abstraction captures key network-level computations, real neurons in the LAL may exhibit more complex intrinsic dynamics — such as oscillatory firing, spontaneous activity, or adaptation — which could influence the circuit's temporal behavior and decision thresholds. Second, although our model already includes most of the highly connected neurons between PFL2/3 and DNs, other neurons may also participate in the pro-goal or anti-goal steering control. For example, AUTO19 or LAL083 were suggested to be part of the central complex steering neurons [40]. Moreover, some neurons may convey information from the mushroom body for the olfaction-driven steering control [40]. Third, our synaptic polarity assignments are based on neurotransmitter predictions from the FlyWire dataset [58], which were generated using machine learning classifier [24,58]. While our assumption that GABA and glutamate are inhibitory aligns with existing Drosophila literature[59], it remains possible that prediction errors or context-dependent transmitter actions could alter the functional logic of the circuit. Moreover, we treated the inhibitory GABA and glutamate as functionally equivalent, but in reality, they may differ in kinetics, receptor mechanisms, or downstream effects. Incorporating more biologically detailed neuron models and experimentally validated neurotransmitter identities will be essential for refining and validating the proposed circuit mechanisms.

Figure legends

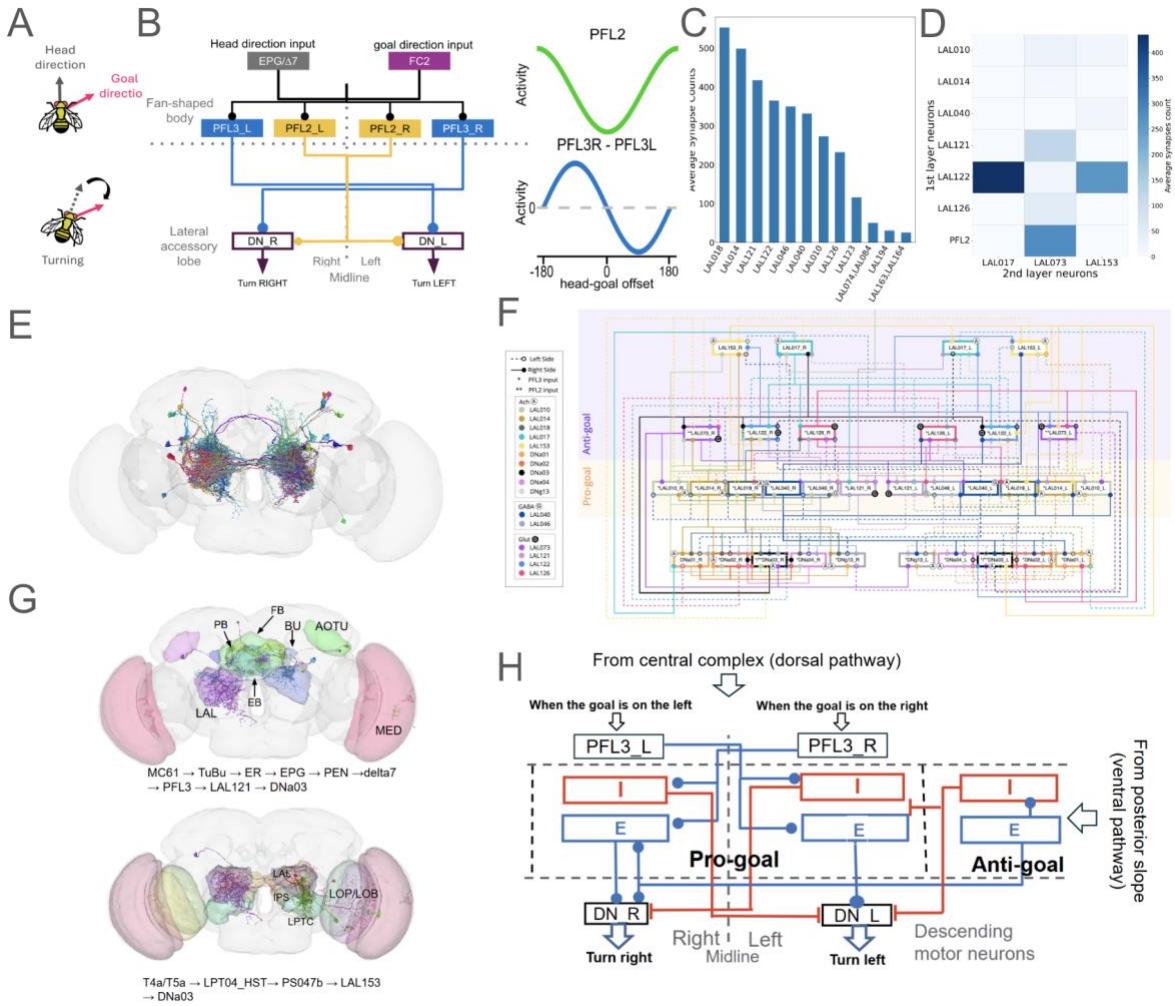

Fig. 1. The goal-directed steering behavior and the associated LAL control circuits in Drosophila melanogaster. A. The present study investigated the neural circuit that modulates goal-directed steering behavior, in which fruit flies rotate their bodies until they face the goal direction. B. (Left) Schematics of the neural circuits for goal-directed steering based on earlier studies [35,36]. The system involves the fan-shaped body (FB) and lateral accessory lobes (LAL), with the output descending neurons (DNs) initiating the body rotation. (Right) The input (heading and goal-direction signals) is processed by the PFL3 and PFL2 neurons, which encode the offset between the heading and goal directions differently (top and bottom). C. The average synapse counts between the PFL3-connected LAL neurons (presynaptic) and the DNa01-04 neurons (postsynaptic). We selected those with counts > 100 to form the first neuron set of the model. D. We discovered a second set of neurons that strongly interact with neurons in the first set. The chart shows the average synapse counts (color-coded) between neurons in the second set and from neurons in the second to the first set. E. The skeletons of neurons modeled in the present model. The skeletons are represented by the tracing lines from the Flywire database [24]. F. The connectome of the modeled neurons, reconstructed from data available at Flywire and hemibrain databases [23]. Each rectangle represents a neuron type and lines represent connections between them. G. The visual information is delivered to the

modeled LAL neurons mainly by two pathways: the dorsal pathway (top) via the central complex and the ventral pathway (bottom) via IPS. The plots show two example paths from the medulla to the descending neurons in the dorsal and ventral pathways. H. Based on the connections and the input pathways, we can classify these neurons into two sub-circuits: pro-goal and anti-goal. Each rectangle represents a small group of neurons with "E" labelling excitatory, while "I" inhibitory. The pro-goal circuit turns the fruit fly toward the goal while the anti-goal circuit turns the fruit fly away from the goal. For visualization purposes, the chart displays a simplified wiring diagram.

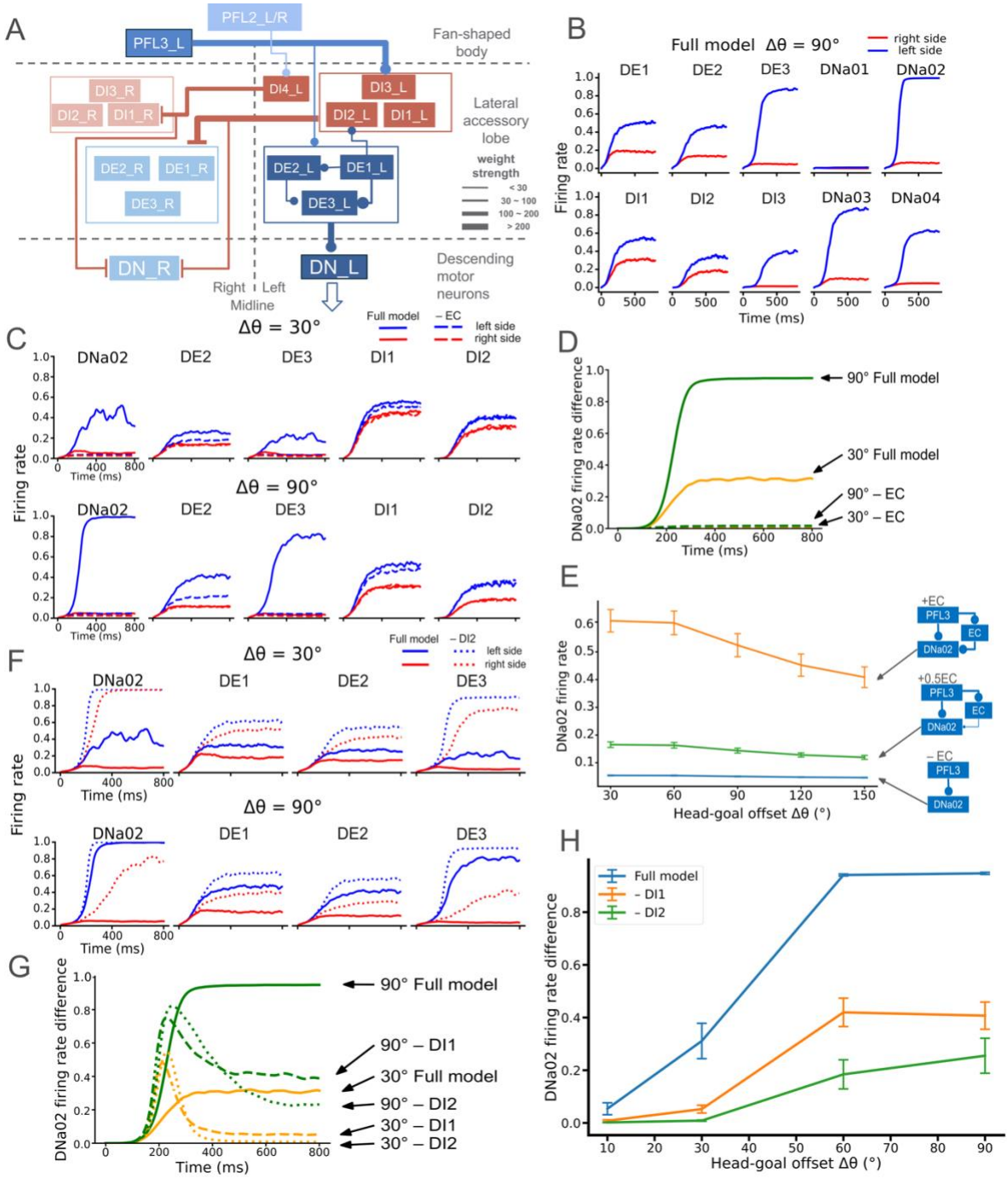

Fig. 2. The pro-goal circuit. A. Schematics of the neurons and major connections in the pro-goal circuit. DE1 (LAL010), DE2 (014) and DE3 (018) form an excitatory core (EC) driving the ipsilateral descending neurons, while DI1 (LAL040) and DI2 (121) inhibit the contralateral pro-goal circuit and descending neurons. The pro-goal circuit is symmetric, but for visual clarity, only connections associated with the left side of the circuit are shown here. B. Mean response of the pro-goal neurons in the model at $\Delta\theta$=90° (head-goal offset) over 50 trials. Most descending neurons exhibit much higher firing rates on the left than on the right side, indicating the motor command to turn left. C. Mear responses of the full model with (solid curves) or without EC (-EC; dashed curves) at $\Delta\theta$=30° (top) or 90° (bottom) over 50 trials. Removing EC from the model results in a largely decreased left-right firing rate difference in many neurons, including the turning command neuron DNa02. D. Mean firing rate difference between left and right DNa02s (

Δr_{DNa02}) at $\Delta\theta$=30° or 90°, with (Full model; solid curves) or without EC (-EC; dashed curves) over 50 trials. E. Mean Δr_{DNa02} (50 trials) as a function of $\Delta\theta$ with full (+EC), 50% (+0.5EC) and 0% (-EC) EC output strengths in an isolated circuit only contains unilateral PFL3, EC and DNa02. EC boosts the activity of DNa02 at all $\Delta\theta$. F. Mean responses (50 trials) of the full model (solid curves) or without the inhibitory DI2 (-DI2; dashed curves). Most neurons are more activated, but the left-right differences are reduced in the absence of DI2. G. Similar to D but with the full model, and DI1 or DI2 removed. H. Similar to E but with the full model and DI1 or DI2 removed. Without DI1 or DI2, Δr_{DNa02} significantly reduces at all $\Delta\theta$.

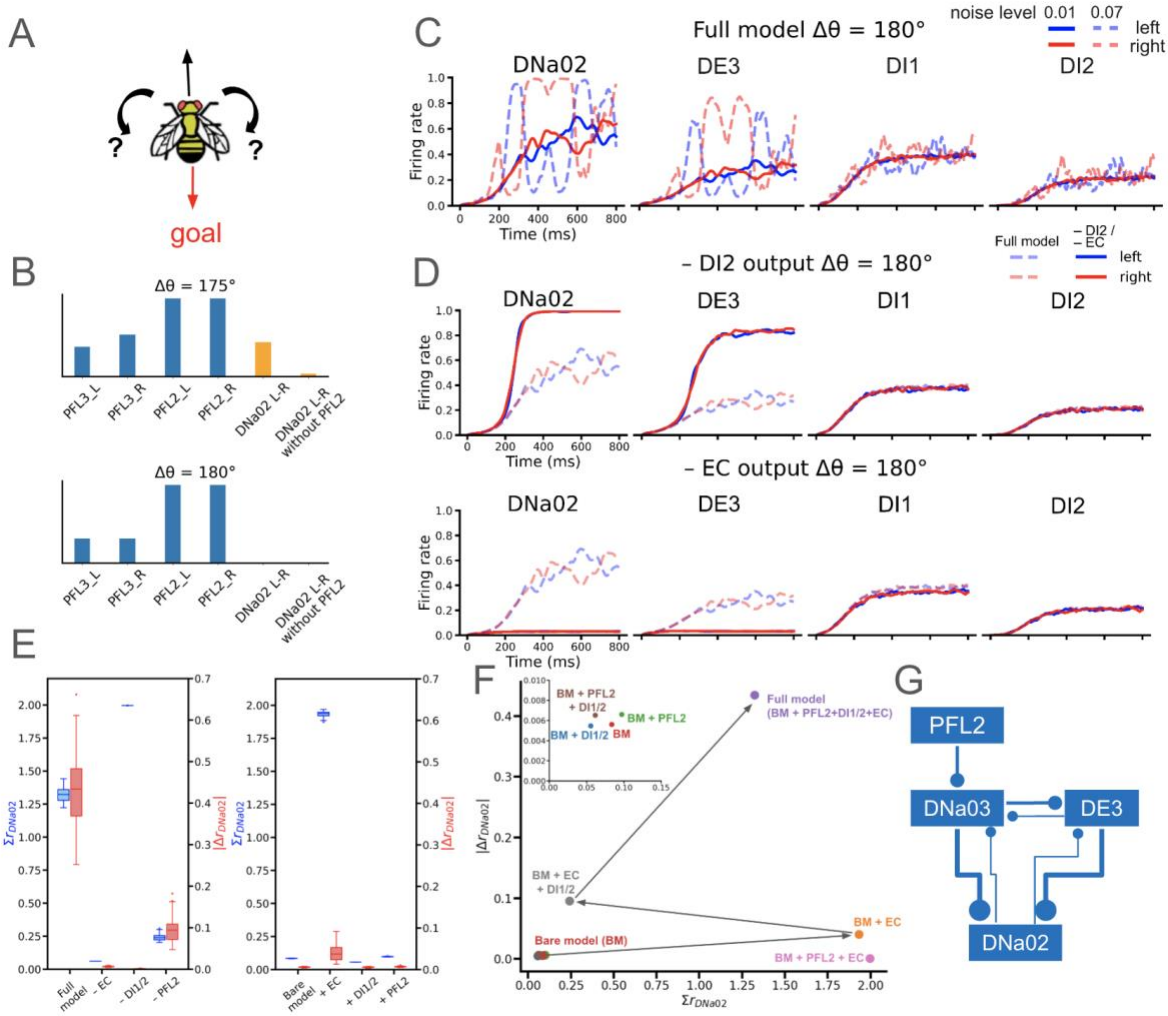

Fig. 3: The Rear Stalemate and how the circuit resolves it. A. A schematic shows that Rear Stalemate occurs when the goal is 180° from the head direction ($\Delta\theta$=180°). In this case, the inputs from PFL3 neurons are symmetric and the responses of DNa neurons are also symmetric, leading to a stalemate without turning. B. Schematics of the effect of PFL2 on Rear Stalemate. (Top) When $\Delta\theta = 175°$, the PFL2 can magnify the slight differences between left and right PFL2 firing rates and increases Δr_{DNa02} . (Bottom) However, when $\Delta\theta$=180°, PFL2 has a very limited effect on Δr_{DNa02} due to the completely symmetric input from both PFL2 and PFL3. C. Sample trials of Rear Stalemate ($\Delta\theta$=180°) and the effect of the noise. In Rear Stalemate ($\Delta\theta$=180°), a small noise (Gaussian noise with standard deviation = 0.01, solid curves) in the system can lead to a large $|\Delta r_{DNa02}|$, which indicates the system's ability to turn away from $\Delta\theta$=180°, or resolve the stalemate. A larger noise (s.t.d. = 0.07, dashed curves) increases $|\Delta r_{DNa02}|$, and therefore can resolve the stalemate more efficiently. D. Sample trials demonstrate the crucial roles of EC (top) and DI2 (bottom) in resolving Rear Stalemate. Without EC and DI2, $|\Delta r_{DNa02}|$ drops to nearly zero. E. (Left) We study the effect of PFL2, EC or DI2 by removing each of them from the full model (averaged across 50 trials). The results indicate that including all three components (the full model) leads to the largest $|\Delta r_{DNa02}|$, while the absence of any one of the components results in a smaller $|\Delta r_{DNa02}|$. (Right) We created a bare model by removing PFL2, EC and DI2 from the full model and add each of the three components back one at a time. F. We summarized the results in E by plotting a Δr_{DNa02} vs. Σr_{DNa02} plot. The arrows illustrate how adding the component one by one to the bare model (BM) maximized Δr_{DNa02} (see text). G. The connections between the PFL2 and DE2 (part of EC) subcircuits. The

interaction created a nonlinear effect that greatly increased the excitation on DNa02 than when only one (PFL2 or EC) acted alone.

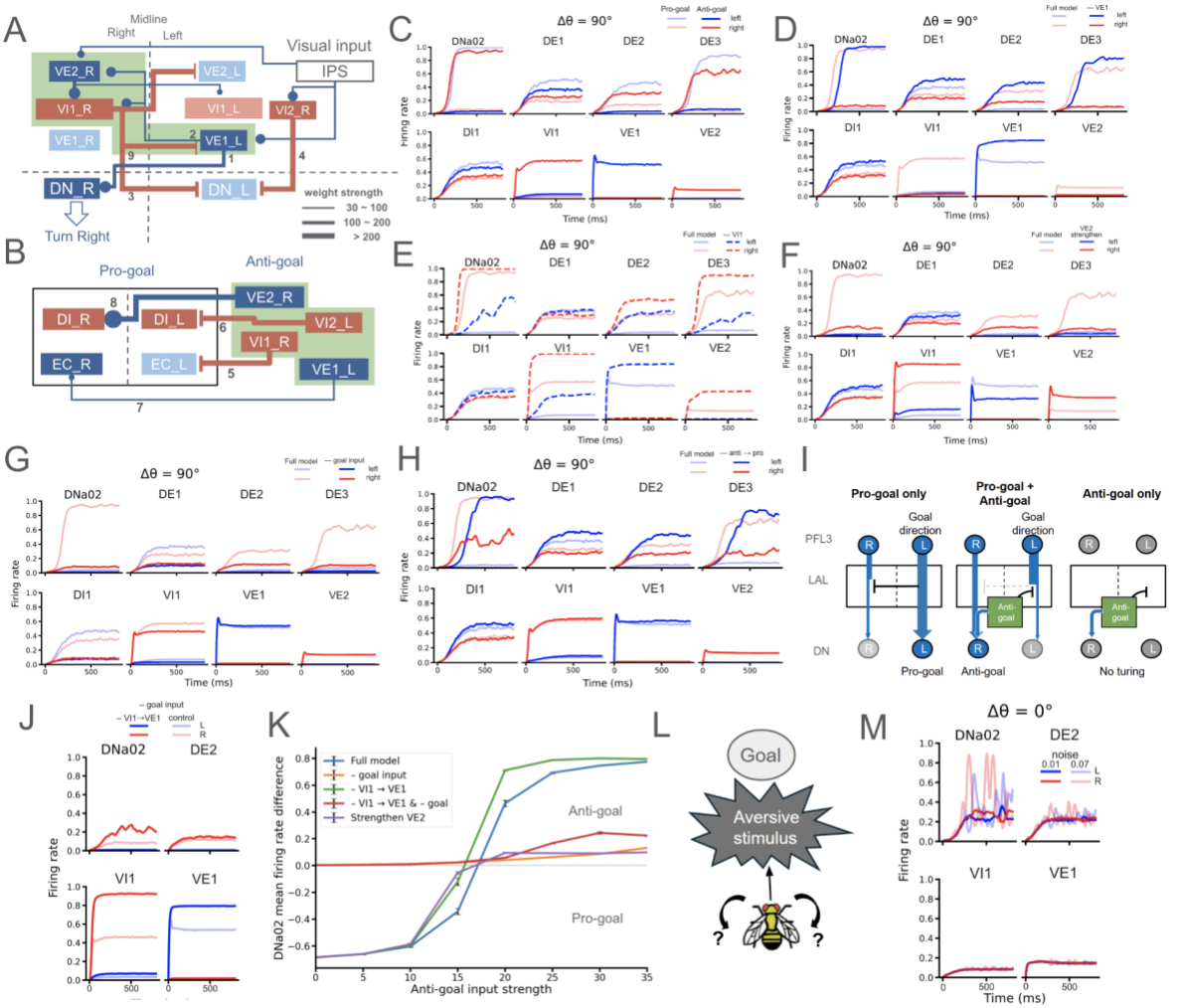

Fig. 4. The anti-goal circuit. A. Schematics of the neurons and major connections in the anti-goal circuit. The circuit is formed by tightly coupled VE1 (LAL153), VE2 (LAL017), VI1 (LAL122) and VI2 (LAL046) neurons. When activated by unilateral input from IPS, VE1 excites contralateral descending neurons, while VI1 and VI2 inhibit the descending neurons subcircuit ipsilateral to the IPS input. B. The major projections from the anti-goal tto the pro-goal neurons. These connections suppress the pro-goal rotation in the ipsilateral side of the IPS input, therefore facilitating the anti-goal (contralateral) turning. The numbers in B & C label the important pathway explained in the text. C. The neural activities in an anti-goal turning (pro-goal $\Delta\theta$ =90° + anti-goal inputs) versus a pro-goal turning (only pro-goal input). D-F. Same as C but with VE1 removed, VI1 removed and VE2's input strengthened, respectively. The manipulations demonstrated the functions of these neurons in the anti-goal response. G. The neural activities in the anti-goal response when no pro-goal input is provided. No anti-goal turning can be elicited without pro-goal input. H. Same as G but with anti-goal to pro-goal neuronal connections removed. The anti-goal turning was abolished in this condition. I. Schematics of the conditioned anti-goal mechanism. Left: With only pro-goal input, the pro-goal neurons in the pro-goal turning side (left) inhibit the response of the contralateral side (right). Middle: When anti-goal input is initiated, the anti-goal circuit suppresses the left pro-goal response, releases the right pro-goal circuit, and further enhances the right turn response. Right: Without the pro-goal input, the anti-goal circuit alone is not sufficient to initiate a turning response. J. The VI1→VE1 connections were important for the conditioned anti-goal mechanism because removing the connections partially rescued the

anti-goal response when no pro-goal input was provided. K. A systematic anti-goal test under several conditions: removing goal input, removing VI1→VE1 connections, removing both and enhancing VE2's input. The model could not make any anti-goal response without the goal input (orange curve) but the anti-goal response was partially rescued if the VI1→VE1 connections were removed. L. The Front Stalemate problem. If an aversive stimulus and the goal both appear right in front of the fly, the input strengths to the bilateral anti-goal circuits are identical, leading to a stalemate condition. M. An anti-goal response can still be triggered in the front stalemate condition, provided that the noise level is sufficiently large.

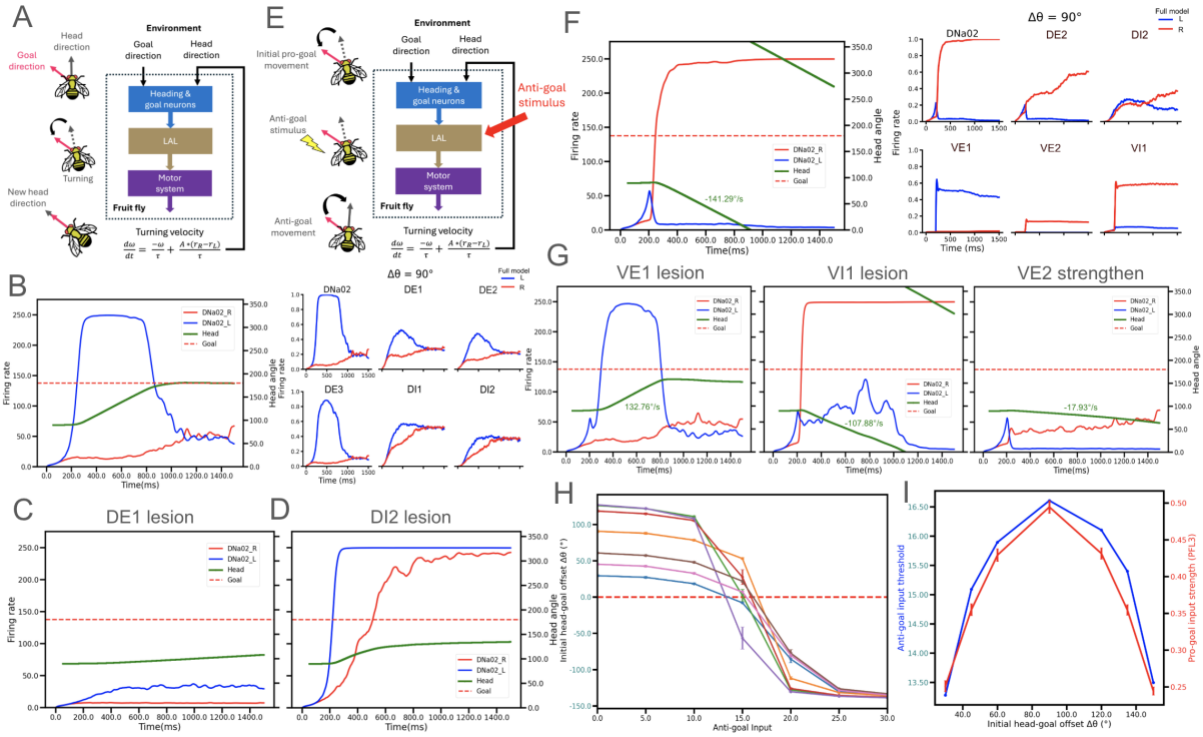

Fig. 5. The performance of the model in closed-loop simulations. A. The block diagram of the closed-loop pro-goal simulations. In each time step the output of the model is transformed into the angular velocity of the fly's body. The new head direction is calculated by integrating the angular velocity. The updated head direction is fed back to the model in the next time step. B. (Left) Example closed-loop simulations of pro-goal turning ($\Delta\theta = 90°$). Driven by the difference between the left (blue) and right (red) DNa02 activity, the heading (green) quickly reached the goal (dashed line) and then stopped. (Right) Firing rate traces of key neurons in the pro-goal circuit. C & D. Example closed-loop simpulations with DE1 and EI2 lesioned, respectively. The lesions greatly reduced the pro-goal turning. E. The block diagram of the closed-loop anti-goal simulations. F. (Left) Example closed-loop simulations of anti-goal turning. The simulation started with a 200ms of pro-goal signals ($\Delta\theta = 90°$) followed by an onset of the anti-goal input, which led to a rapid turn away from the goal with the turning rate labeled (number in green). (Right) Firing rate traces of key neurons in the anti-goal circuit. G. Effects of the key neurons in the anti-goal tests. (Left) Lesion of VE1 abolished the anti-goal response and the system performed a pro-goal turning. (Middle) Lesion of VI1 was not abolished but moderately slowed down the anti-goal turning. (Right) Strengthen the VE2 output greatly reduced the anti-goal response. H. Responses of the model with various initial $\Delta\theta$ (color coded line) under different anti-goal input strengths. Anti-goal responses were only triggered when the anti-goal input was stronger than certain threshold values. I. The threshold anti-goal input value was dependent on the initial $\Delta\theta$. This dependency closely followed the strength of the pro-goal input (from PFL3) at the initial $\Delta\theta$.

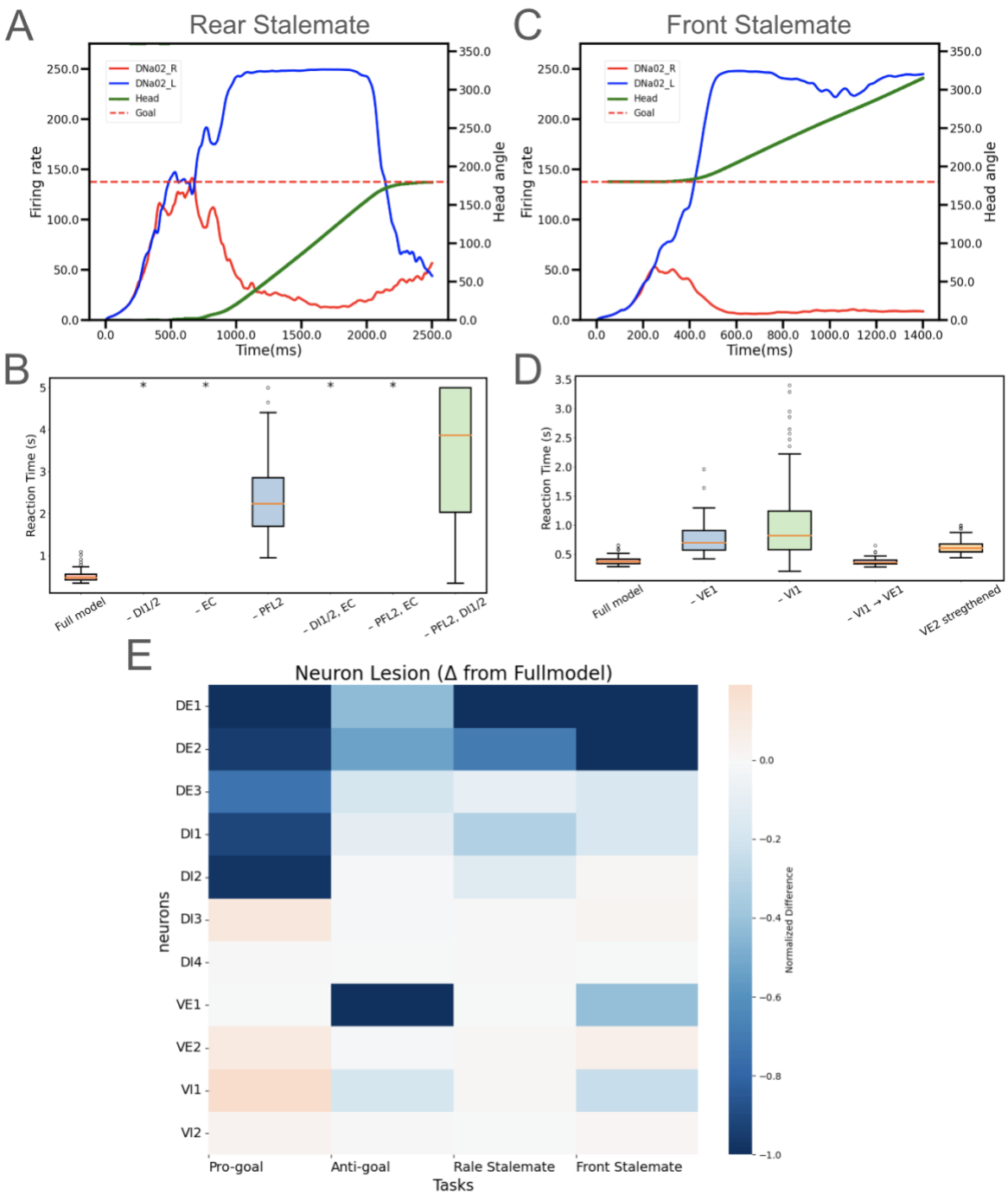

Fig. 6: Closed-loop simulations for Rare & Front Stalemate. A. An example trial for Rear Stalemate. The model took about 500 milliseconds to resolve the stalemate and quickly turned into the goal afterwards. B. Lesion tests of the key pro-goal neurons in Front Stalemate in the pro-goal task (trial number = 100 for each condition). Removing EC, DI or PFL2, or any two of them led to a greatly prolonged pro-goal reaction time. C. An exmpale trial for Front Stalemate. The model took about 400 milliseconds to resolve the stalemate and quickly turned away from the goal direction. D. Lesion tests of the key anti-goal neurons in Rear Stalemate in the anti-goal task (trial number = 100 for each condition). Removing VE1, VI1, or strengthening VE2 output connections led to increased anti-goal reaction time. However, removing the VI1 à VE1 connection led to little changes in the reaction time, which was consistent with the results from Fig 4J & 4K. E. Systematic tests of the effects of

every neuron in the model in pro-goal, anti-goal, Rear Stalemate and Front Stalemate. We performed 30 trials for each condition in the open-loop test and computed the difference in the mean Δr_{DNa02} between the lesion condition and the control condition (full model without lesion). The results are color coded. Positive values indicate that the lesion improves the response of the task, while negative values indicate reduced responses.

Methods and Materials

The connectome data and neuron selection

The identity of neurons, connections between neurons, and the connection weights of the proposed model were retrieved from Flywire[24], an electrical microscopy-based *Drosophila* connectome database. We assume that the connection weight between two neurons is proportional to the number of synapses between them.
We also checked the hemibrain[60] and found that the connections between the neurons and the relative weights are consistent with the Flywire database. However, most neurons in the proposed model cross the midline, while hemibrain provides data for neurons in one hemisphere, except for the central complex. Therefore, the proposed model was built primarily based on data from Flywire.

In the present study, we investigate the role of the lateral accessory lobe (LAL) in the goal-directed turning behavior (Fig. 1A). Therefore, we focused on the LAL neurons that mediate the signal transmission between the head- and goal-direction encoding neurons and the descending motor neurons. Out of more than 2212 neurons innervating each side of LAL, we performed selection criteria to focus our analysis on a small but essential subset of neurons, which include 12 PFL2 neurons, 24 PFL3 neurons, 22 LAL neurons, and 8 DNa neurons. See Results for details.

The neuron model

The LAL model was built and simulations were performed using the Brian2 simulator[61]. The input sources of the LAL model were PFL3 and PFL2 neurons (for the pro-goal circuit), and IPS (for the anti-goal circuit). The PFL3 model in the present study was developed based on Mussells Pires et al. 2022[36], which suggested that the PFL3 neurons received inputs from both head direction (EPG and Δ7) and goal direction (FC2) neurons. Both neuron groups generated sinusoidal signals as inputs to PFL3 neurons. Following Mussells Pires et al. 2022[36], we modeled the firing rate r_i of a PFL3 neuron i by:

$$\frac{dr_i}{dt} = \frac{-r_i}{\tau} + a\log(1 + \exp(b(\sum_j w_{ij} r(H)_j^{head} + c\sum_k g_{ik} r(G)_k^{FC2} + d))).$$

The superscripted R/L denotes the right (R) or left (L) side PFL3, H is the heading angle, G is the goal direction. $r(H)_j^{head}$ are the head-direction encoding neuron with the synaptic weights w_{ij}, $r(G)_k^{FC2}$ are the goal-direct encoding FC2 neurons with the synaptic weights g_{ik}, and c (=0.67) is a parameter for modifying the relative strength between heading and goal direction signal. The rest parameters, a (=22.09 Hz), b (=2.33) and d (=-0.52), also followed the values used in Mussells Pires et al. 2022[36].

Unlike PFL3 neurons, which innervate the contralateral LALs, PFL2 neurons innervate bilateral LALs[24,35,60]. The firing rate r_i of the *i*-th PFL2 is given by:

$$\frac{dr_i}{dt} = \frac{-r_i}{\tau} + \frac{1}{(1 + exp(-\alpha * (r_i^{head} + r_i^{FC2} - \beta))) * \tau}$$

The firing rates r for all other neurons except for PFL3 and PFL2 are given by:

$$\frac{dr}{dt} = \frac{-r}{\tau} + \frac{1}{(1 + exp(-\alpha(I_{syn} + I_{task} - \beta))) * \tau}$$

where τ=10ms is the time constant of the neuron, α and β are parameters for the sigmoidal activation function, I_{sys} is the synaptic current from other neurons, I_{task} is task protocal related inputs from outside the LAL circuits.

The synaptic current I_{syn} for each neuron is determined by:

$$I_{sys} = \sum_{i} f_t w_i r_i$$

where r_i is the firing rate of the i-th input neuron and w_i is the associated synaptic weight, which is positive for an excitatory input and negative for an inhibitory input. The synaptic weights were determined based on the Flywire database. For each pair of connected neurons, we calculated the mean synapse number on the left and right sides of the brain and used this mean value in the model, assuming that the circuits were generally symmetric. The variable f_t is a factor dependent on the type of neurotransmitter *t*. All the model neurons are predicted (by the Flywire database) to be one of the three neurotransmitter types: cholinergic (Ach) (PFL3, DE1, DE2, DE3, VE1, VE2 and all the DNs), GABAergic ($GABA_A$) neurons (DI1, and VI2) and Glutaminergic (Glut) (DI2, DI3, DI4, and VI1)(Supplementary Table 2). While cholinergic and GABAergic receptors are known to be excitatory and inhibitory, respectively, we assumed that the glutaminergic neurons are inhibitory in the present study based on previous studies on the *Drosophila* neurotransmitters[24,58].

The model tuning

The proposed model was highly constrained by the conntecome data. Only three parameters were tuned during model development. The first is the neurotransmitter factor f_t, which was determined through parameter sweeping. The optimal values (ACh = 0.2, GABA = 0.09, Glutamate = 0.04) were those maximizing left-right firing rate difference of the descending neurons DNa02 at 90° goal–head direction offset in the open-loop pro-goal task. The other two tuning parameters are α and β, which define the shape of an activation function. The parameter β defines the input level that drives the neuron to half of its maximum firing rate, while α defines the slope at this point. The parameters α and β were determined based on a homeostatic hypothesis: a neuron would adjust its response so that its firing rate ($r = 0{\sim}1$) roughly matches the dynamical range of the input (from no input to maximum excitatory input). Based on this assumption, we set β of a neuron roughly equal to half of its maximum excitatory input. But for the sake of model simplicity, which means reducing the number of distinct parameter values, we did not set each β to the exact value stated above, but to the closest value from the following representative numbers: 18, 20, 50, and 120. See Table 2 for details. The parameter α was set to equal to $5/\beta$, or αβ = 5. Thses settings made $r \approx 0.99$ at its maximum excitatory input, and $r \approx 0.5$ at its half excitatory input. The weight of each synapse was computed as the mean of the left and right synapse counts to ensure the symmetry of the circuit. Gaussian noise was applied to PFL3 and PFL2 populations, and the additional inputs introduced under anti-goal conditions were also perturbed with Gaussian noise. The noise equation $\sigma\sqrt{\frac{2}{\tau}}\xi$, where σ control noise strengh, $\tau = 10$ ms, ξ means Gaussian white noise in Brian2.

Table 2. The parameters for each neuron model

Neuron	α	β	Neuron	α	β
DE1	0.25	18	VI2	0.25	20
DE2	0.25	18	VE1	0.25	20
DE3	0.25	18	VE2	0.25	20
DI1	0.1	50	DNa01	0.25	20
DI2	0.05	120	DNa02	0.1	50
DI3	0.25	20	DNa03	0.1	50
DI4	0.25	20	DNa04	0.1	50
VI1	0.25	20	DNg13	0.25	20

The closed-loop system

In the closed-loop system, the output of the model changes the head direction, which was fed back to the circuit model in the closed-loop experiment. Specifically, in each timestep of the simulation, the instantaneous turning velocity is determined by Δr_{DNa02} (right-left DNa02 firing rate difference) and a new head direction at the end of the timestep is computed based on the velocity. The new head direction is fed back to the neural circuit to generate new PFL2 and PFL3 input and subsequently produce a new Δr_{DNa02} for the next timestep.

The angular velocity of body turning is computed by:

$$\frac{d\omega}{dt} = \frac{-\omega}{\tau} + \frac{A * (r_{DNa02_R} - r_{DNa02_L})}{\tau}$$

where ω is the angular velocity, τ=20ms, A = 0.15 is the gain that adjusts the relation between angular velocity and descending neuron activity, and r_{DNa02_R} / r_{DNa02_L} mean the firing rate of right and left DNa02 neurons respectively.

Data availability

This is a theoretical study based on Flywire and hemibrain, which are publicly available connectome databases.

Code availability

The code used in the present study will be made publicly available after the manuscript is published in a peer-reviewed journal.

Acknowledgements

C.-C. Liao thanks Dr. Ching-Che Charng for insightful discussions. C.-C. Lo thanks Dr. Ann-Shyn Chiang for advice and discussions. This work was supported by the National Science and Technology Council grants 111-2311-B-007-011-MY3, 114-2311-B-007-016-MY3, and 114-2321-B-002-027, and by the Brain Research Center under the Higher Education Sprout Project, co-funded by the Ministry of Education in Taiwan.

Author Contribution

C.-C. Liao wrote the code, performed simulations and analysis, produced figures and wrote the manuscript. C. N. participated in the early phase of the study by writing the code, performing simulations and preparing figures. Y.-Sh. Liu wrote the manuscript and contributed the intellectual content through discussion. C.-C. Lo designed and supervised the study, wrote and finalized the manuscript.

Competing interests

The authors declare no competing interests.

References

1. Freas, C. A. & Cheng, K. The Basis of Navigation Across Species. *Annual Review of Psychology* **73**, 217–241 (2022).
2. Poulter, S., Hartley, T. & Lever, C. The Neurobiology of Mammalian Navigation. *Current Biology* **28**, R1023–R1042 (2018).
3. Wilson, R. I. Neural Networks for Navigation: From Connections to Computations. *Annual Review of Neuroscience* **46**, 403–423 (2023).

4. O'Keefe, J. & Dostrovsky, J. The hippocampus as a spatial map. Preliminary evidence from unit activity in the freely-moving rat. *Brain Research* **34**, 171–175 (1971).
5. Hafting, T., Fyhn, M., Molden, S., Moser, M.-B. & Moser, E. I. Microstructure of a spatial map in the entorhinal cortex. *Nature* **436**, 801–806 (2005).
6. Taube, J. S., Muller, R. U. & Ranck, J. B. Head-direction cells recorded from the postsubiculum in freely moving rats. I. Description and quantitative analysis. *J. Neurosci.* **10**, 420–435 (1990).
7. Sanders, H., Rennó-Costa, C., Idiart, M. & Lisman, J. Grid Cells and Place Cells: An Integrated View of their Navigational and Memory Function. *Trends in Neurosciences* **38**, 763–775 (2015).
8. Tolman, E. C. Cognitive maps in rats and men. *Psychological Review* **55**, 189–208 (1948).
9. Basu, J. & Nagel, K. Neural circuits for goal-directed navigation across species. *Trends in Neurosciences* **47**, 904–917 (2024).
10. Basu, R. *et al.* The orbitofrontal cortex maps future navigational goals. *Nature* **599**, 449–452 (2021).
11. Beetz, M. J., Kraus, C. & el Jundi, B. Neural representation of goal direction in the monarch butterfly brain. *Nat Commun* **14**, 5859 (2023).
12. Goulard, R., Heinze, S. & Webb, B. Emergent spatial goals in an integrative model of the insect central complex. *PLOS Computational Biology* **19**, e1011480 (2023).
13. Franklin, D. W. & Wolpert, D. M. Computational Mechanisms of Sensorimotor Control. *Neuron* **72**, 425–442 (2011).
14. Brembs, B. The brain as a dynamically active organ. *Biochemical and Biophysical Research Communications* **564**, 55–69 (2021).

15. Ardid, S. & Wang, X.-J. A Tweaking Principle for Executive Control: Neuronal Circuit Mechanism for Rule-Based Task Switching and Conflict Resolution. *J. Neurosci.* **33**, 19504–19517 (2013).

16. Lo, C.-C. & Wang, X.-J. Conflict Resolution as Near-Threshold Decision-Making: A Spiking Neural Circuit Model with Two-Stage Competition for Antisaccadic Task. *PLOS Comput Biol* **12**, e1005081 (2016).

17. Watanabe, M. & Munoz, D. P. Neural correlates of conflict resolution between automatic and volitional actions by basal ganglia. *European Journal of Neuroscience* **30**, 2165–2176 (2009).

18. Moser, E. I., Kropff, E. & Moser, M.-B. Place cells, grid cells, and the brain's spatial representation system. *Annu Rev Neurosci* **31**, 69–89 (2008).

19. Giocomo, L. M., Moser, M.-B. & Moser, E. I. Computational Models of Grid Cells. *Neuron* **71**, 589–603 (2011).

20. Taube, J. S. The Head Direction Signal: Origins and Sensory-Motor Integration. *Annual Review of Neuroscience* **30**, 181–207 (2007).

21. Shih, C.-T. *et al.* Connectomics-Based Analysis of Information Flow in the Drosophila Brain. *Current Biology* **25**, 1249–1258 (2015).

22. Shih, C.-T. *et al.* Diverse Community Structures in the Neuronal-Level Connectome of the Drosophila Brain. *Neuroinform* **18**, 267–281 (2020).

23. Scheffer, L. K. *et al.* A connectome and analysis of the adult Drosophila central brain. *eLife* **9**, e57443 (2020).

24. Dorkenwald, S. *et al.* FlyWire: online community for whole-brain connectomics. *Nat Methods* **19**, 119–128 (2022).

25. Seelig, J. D. & Jayaraman, V. Neural dynamics for landmark orientation and angular path integration. *Nature* **521**, 186–191 (2015).

26. Su, T.-S., Lee, W.-J., Huang, Y.-C., Wang, C.-T. & Lo, C.-C. Coupled symmetric and asymmetric circuits underlying spatial orientation in fruit flies. *Nature Communications* **8**, 139 (2017).

27. Kim, S. S., Rouault, H., Druckmann, S. & Jayaraman, V. Ring attractor dynamics in the *Drosophila* central brain. *Science* **356**, 849–853 (2017).

28. Chang, N., Huang, H.-P. & Lo, C.-C. Global inhibition in head-direction neural circuits: a systematic comparison between connectome-based spiking neural circuit models. *J Comp Physiol A* https://doi.org/10.1007/s00359-023-01615-z (2023) doi:10.1007/s00359-023-01615-z.

29. Han, R. *et al.* Coordination through Inhibition: Control of Stabilizing and Updating Circuits in Spatial Orientation Working Memory. *eNeuro* **8**, (2021).

30. Pisokas, I., Heinze, S. & Webb, B. The head direction circuit of two insect species. *eLife* **9**, e53985 (2020).

31. Fisher, Y. E., Marquis, M., D'Alessandro, I. & Wilson, R. I. Dopamine promotes head direction plasticity during orienting movements. *Nature* **612**, 316–322 (2022).

32. Kim, S. S., Hermundstad, A. M., Romani, S., Abbott, L. F. & Jayaraman, V. Generation of stable heading representations in diverse visual scenes. *Nature* **576**, 126–131 (2019).

33. Fisher, Y. E., Lu, J., D'Alessandro, I. & Wilson, R. I. Sensorimotor experience remaps visual input to a heading-direction network. *Nature* **576**, 121–125 (2019).

34. Okubo, T. S., Patella, P., D'Alessandro, I. & Wilson, R. I. A Neural Network for Wind-Guided Compass Navigation. *Neuron* **107**, 924-940.e18 (2020).

35. Westeinde, E. A. *et al.* Transforming a head direction signal into a goal-oriented steering command. *Nature* **626**, 819–826 (2024).

36. Mussells Pires, P., Zhang, L., Parache, V., Abbott, L. F. & Maimon, G. Converting an allocentric goal into an egocentric steering signal. *Nature* **626**, 808–818 (2024).

37. Lyu, C., Abbott, L. F. & Maimon, G. A neuronal circuit for vector computation builds an allocentric traveling-direction signal in the Drosophila fan-shaped body. *bioRxiv* 2020.12.22.423967 (2020) doi:10.1101/2020.12.22.423967.

38. Namiki, S., Dickinson, M. H., Wong, A. M., Korff, W. & Card, G. M. The functional organization of descending sensory-motor pathways in Drosophila. *eLife Sciences* **7**, e34272 (2018).

39. Kottler, B., Faville, R., Bridi, J. C. & Hirth, F. Inverse Control of Turning Behavior by Dopamine D1 Receptor Signaling in Columnar and Ring Neurons of the Central Complex in Drosophila. *Current Biology* **29**, 567-577.e6 (2019).

40. Rayshubskiy, A. *et al. Neural Circuit Mechanisms for Steering Control in Walking Drosophila*. 2020.04.04.024703 https://www.biorxiv.org/content/10.1101/2020.04.04.024703v2 (2020) doi:10.1101/2020.04.04.024703.

41. Yang, H. H. *et al. Fine-Grained Descending Control of Steering in Walking* Drosophila. http://biorxiv.org/lookup/doi/10.1101/2023.10.15.562426 (2023) doi:10.1101/2023.10.15.562426.

42. Brezovec, B. E. *et al.* Mapping the neural dynamics of locomotion across the Drosophila brain. *Current Biology* **34**, 710-726.e4 (2024).

43. Cheong, H. S. J. *et al.* Transforming descending input into behavior: The organization of premotor circuits in the Drosophila Male Adult Nerve Cord connectome. 2023.06.07.543976 Preprint at https://doi.org/10.1101/2023.06.07.543976 (2024).

44. Cruz, T. L. & Chiappe, M. E. Multilevel visuomotor control of locomotion in *Drosophila*. *Current Opinion in Neurobiology* **82**, 102774 (2023).

45. Chiappe, M. E. Circuits for self-motion estimation and walking control in Drosophila. *Current Opinion in Neurobiology* **81**, 102748 (2023).

46. Braitenberg, V. *Vehicles: Experiments in Synthetic Psychology*. (MIT Press, 1986).

47. Gattuso, H. C. *et al.* Inhibitory control explains locomotor statistics in walking *Drosophila*. *Proc. Natl. Acad. Sci. U.S.A.* **122**, (2025).

48. Feng, K. *et al.* A central steering circuit in Drosophila. 2024.06.27.601106 Preprint at https://doi.org/10.1101/2024.06.27.601106 (2024).

49. Yang, H. H. *et al.* Fine-grained descending control of steering in walking Drosophila. *Cell* **187**, 6290-6308.e27 (2024).

50. Wei, H., Kyung, H. Y., Kim, P. J. & Desplan, C. The diversity of lobula plate tangential cells (LPTCs) in the Drosophila motion vision system. *J Comp Physiol A* **206**, 139–148 (2020).

51. Burridge, K. & Wennerberg, K. Rho and Rac Take Center Stage. *Cell* **116**, 167–179 (2004).

52. Jilkine, A. & Edelstein-Keshet, L. A Comparison of Mathematical Models for Polarization of Single Eukaryotic Cells in Response to Guided Cues. *PLOS Computational Biology* **7**, e1001121 (2011).

53. Lahav, G. *et al.* Dynamics of the p53-Mdm2 feedback loop in individual cells. *Nat Genet* **36**, 147–150 (2004).

54. Vousden, K. H. & Prives, C. Blinded by the Light: The Growing Complexity of p53. *Cell* **137**, 413–431 (2009).

55. Collier, J. R., Monk, N. A. M., Maini, P. K. & Lewis, J. H. Pattern Formation by Lateral Inhibition with Feedback: a Mathematical Model of Delta-Notch Intercellular Signalling. *Journal of Theoretical Biology* **183**, 429–446 (1996).

56. Sprinzak, D. *et al.* Cis-interactions between Notch and Delta generate mutually exclusive signalling states. *Nature* **465**, 86–90 (2010).

57. Shaya, O. & Sprinzak, D. From Notch signaling to fine-grained patterning: Modeling meets experiments. *Current Opinion in Genetics & Development* **21**, 732–739 (2011).

58. Eckstein, N. *et al.* Neurotransmitter classification from electron microscopy images at synaptic sites in Drosophila melanogaster. *Cell* **187**, 2574-2594.e23 (2024).

59. Liu, W. W. & Wilson, R. I. Glutamate is an inhibitory neurotransmitter in the Drosophila olfactory system. *PNAS* 201220560 (2013) doi:10.1073/pnas.1220560110.

60. Hulse, B. K. *et al.* A connectome of the Drosophila central complex reveals network motifs suitable for flexible navigation and context-dependent action selection. *eLife* **10**, e66039 (2021).

61. Stimberg, M., Brette, R. & Goodman, D. F. Brian 2, an intuitive and efficient neural simulator. *eLife* **8**, e47314 (2019).